









## Removal of methyl violet dye by a photocatalytic process using variations of TiO<sub>2</sub>/zeolite synthesized from muscovite raw material

Husnul Fatimah<sup>1</sup>, Paulina Taba<sup>1\*</sup>, St. Fauziah<sup>1</sup>, Abdul Karim<sup>1</sup>, Syarifuddin Liong<sup>1</sup>, Syahrudin Kasim<sup>1</sup>, Sahrul<sup>1</sup>, Nur Akifah Pardan<sup>1</sup>

<sup>1</sup> Department of Chemistry, Faculty of Mathematics and Natural Sciences, Hasanuddin University, Makassar, Indonesia

\* Corresponding author's e-mail: paulinataba@unhas.ac.id

### ABSTRACT

The removal of methyl violet dye through a photocatalytic process has been successfully carried out. This study aimed to evaluate the photocatalytic efficiency of TiO<sub>2</sub>/zeolite catalysts in degrading methyl violet dye. Zeolites were synthesized from silica and aluminum sources derived from muscovite raw materials using the hydrothermal method, resulting in two types of zeolites: cancrinite (CAN) in synthesis A and analcime (ANA) in synthesis B. The zeolites were combined with anatase-phase TiO<sub>2</sub> to form photocatalysts, with XRD analysis confirming the cubic structure of analcime and hexagonal cancrinite in the anatase phase. FTIR spectra showed sharp bands in the 468–1005 cm<sup>-1</sup> wave number range. SEM analysis showed that TiO<sub>2</sub>/analcime exhibited a hexagonal morphology with a crystal size of 10.58 μm, while TiO<sub>2</sub>/cancrinite had a rod-shaped morphology with a crystal size of 21.3 μm. Surface area analysis showed that TiO<sub>2</sub>/ANA and TiO<sub>2</sub>/CAN had surface areas of 34.80 m<sup>2</sup>/g and 23.08 m<sup>2</sup>/g, respectively, with pore diameters > 2 nm, which confirmed their mesoporous nature based on the BJH method. UV-DRS analysis showed band gap energies of 3.13 eV for TiO<sub>2</sub>/ANA and 3.11 eV for TiO<sub>2</sub>/CAN. Photodegradation tests showed that the TiO<sub>2</sub>/ANA catalyst exhibited higher methyl violet degradation efficiency than TiO<sub>2</sub>/CAN. This study highlighted the potential of TiO<sub>2</sub>/zeolite-based photocatalysts for effective treatment of dye-contaminated wastewater, contributing to environmental sustainability.

**Keywords:** methyl violet, TiO<sub>2</sub> semiconductor, muscovite raw materials, TiO<sub>2</sub>/ANA, TiO<sub>2</sub>/CAN.

### INTRODUCTION

Textile factories, paint, fabric dyeing, paper production, and printing are just a few industries that use synthetic dyes. When discharged into the environment, they can be associated with more severe health problems, including respiratory problems and hormone disruption. Synthetic dyes produce organic pollutants, cause allergic dermatitis and skin irritation, and may increase the risk of cancer (Berradi, et al., 2019). Organic pollutants can negatively impact the environment through contamination from wastewater that contains dyes, including methyl violet (Sadiku, et al., 2022).

The synthetic dye methyl violet comes in various forms, such as tetramethyl (2B), pentamethyl (6B), and hexamethyl (10B) pararosanine.

Compared to 6B and 2B, methyl violet 10B has a darker color intensity. Water, ethanol, diethylene glycol, and dipropylene glycol can all dissolve methyl violet (Bouasla, et al., 2010). It is stable at room temperature, but can break down under prolonged exposure to sunlight, depending on the percentage of UV radiation from the sun (Jeyasubramaniana, et al., 2015).

Water cannot naturally destroy synthetic dyes, so these dyes persist in the environment and can contribute to long-term pollution (Aichour, et al., 2021). Treatment of dyes derived from textile waste with modern methods such as biological treatment (Singh, et al., 2022), coagulation-flocculation (Ihaddaden, et al., 2022), biochar/iron oxide (Zhang, et al., 2020), surfactant-modified biomass (Karaman, et al., 2022), modified magnetic nanosorbents (Perwez, et al., 2022), adsorption (Isik, et

al., 2022), chlorination treatment (Nikraves, et al., 2020), Fenton process (Bouasla, et al., 2010) and photocatalytic (Zhuang, et al., 2022; Hu, et al., 2018). Among these methods, semiconductor-based photocatalysis is promising, because it can convert various organic pollutants into less toxic compounds without using expensive oxidants.

The most effective semiconductor is Titanium dioxide ( $\text{TiO}_2$ ), because it is biologically and chemically inert, non-toxic, in addition to having relatively large band gap energy (3.2 eV) (Zhuang, et al., 2022), long-term chemical stability, and good photon stability (Dharma, et al., 2022). The photocatalytic method works with the formation of positive electron pairs and holes ( $e^-$ ,  $h^+$ ) (Zhou, et al., 2024). Valence band electrons are induced to move to the conduction band by photon energy from sunlight or ultraviolet light, which results in holes in the valence band. When the hole reacts with water, hydroxyl radicals are created. Environmentally benign chemicals like  $\text{CO}_2$  and  $\text{H}_2\text{O}$  are produced by the photocatalytic process (Porcu, et al., 2022)

Surface modification of photocatalysts with supporting materials can improve photocatalytic efficiency (Katwal, et al., 2021), such as glass beads (Zhang, et al., 2020), fiberglass (Huang, et al., 2017), silica (Pal, et al., 2016), alumina (Kim et al., 2022), and zeolite (Huayna, et al., 2024). Among the various supports for photocatalysis, zeolite is a more effective material, because it has a unique uniform pore size (Derbe, et al., 2021). Zeolite is an aluminosilicate compound consisting of two types: natural and synthetic. Synthetic zeolite can be made from muscovite raw materials containing silica and alumina (Khaleque, et al., 2020), such as bentonite and kaolinite (Maj and Matus, 2023).

In this study, alumina and silica were obtained from muscovite raw materials to make synthetic zeolite using the hydrothermal method. The synthesized zeolite was composited with an anatase  $\text{TiO}_2$  semiconductor to form a photocatalyst that increased the photocatalytic efficiency and degraded methyl violet dye.

## METHODS

### Preparation of activation muscovite raw materials

Muscovite raw materials were crushed and sieved using a 200-mesh sieve. The samples were

then stirred in 200 mL of distilled water at room temperature for 30 minutes, filtered, and the precipitate was oven-dried at 100 °C for 2 hours before being dried and stored for further processing (Doğaroğlu et al., 2023). Muscovite raw materials were activated using 1 M HCl, where a 50-gram sample was soaked in the acid for 3 hours, washed, and neutralized to pH 7 with distilled water. The neutralized samples were dried at 100 °C for 2 hours and calcined at 500 °C for 4 hours to prepare them for further applications (Velarde et al., 2023).

### Zeolite synthesis from muscovite raw materials

The synthesis process involved mixing 18 g of  $\text{H}_2\text{O}$  with 1.08 g (Synthesis B) and 2.52 g (Synthesis A) of sodium hydroxide. Muscovite raw materials was added in quantities of 0.82 g and 0.76 g, respectively. The mixtures were placed in an autoclave, sealed tightly, and heated at 170 °C for 72 hours. The resulting solids were vacuum-filtered and rinsed with distilled water until the filtrate reached a neutral pH. Finally, the products were dried at 110 °C for 24 hours.

### Fusing $\text{TiO}_2$ and synthetic zeolite

To prepare the  $\text{TiO}_2$ /zeolite composite, 4 g of  $\text{TiO}_2$  and 10 g of synthetic zeolite were mixed with 21 mL of 96% ethanol in a 250 mL glass beaker. The mixture was ground using an agate mortar and then sonicated for 30 minutes. It was subsequently heated at 110 °C for 3 hours in an oven, followed by calcination at 550 °C for 2 hours in a furnace. After calcination, the solids were ground into a fine powder.

### Characterization of the photocatalyst

The prepared samples were characterized using various analytical instruments. The elemental composition of the muscovite raw material and photocatalyst was analyzed using a Shimadzu EDX-720 spectrometer via X-ray fluorescence (XRF). X-ray diffraction patterns were recorded by a Shimadzu XRD-7000 diffractometer via X-ray diffraction (XRD), using  $\text{Cu K}\alpha$  radiation ( $\lambda=1.5405 \text{ \AA}$ ) in the  $2\theta$  range between 20° to 80°. The band gap energies of the samples were determined using a Thermo Scientific Evolution 220 UV-DRS spectrophotometer. Bond-type analysis was performed by Fourier transform infrared (FTIR) using a Shimadzu IR Prestige 21 FTIR

spectrometer, with spectra recorded in the range of 400–4000  $\text{cm}^{-1}$ . Crystal morphology and diameter were analyzed using scanning electron microscopy-energy dispersive spectroscopy (SEM-EDS) by means of a HITACHI S-4800. In addition, the  $\text{N}_2$  adsorption-desorption isotherms of the synthesized samples were characterized using a surface area analyzer (SAA) Micro 200 to determine the specific surface area using the Brunauer-Emmett-Teller (BET) method. The pore volume and average pore radius were analyzed using desorption isotherms via the Barrett-Joyner-Halenda (BJH) method to determine the pore size distribution.

### Photocatalytic test

A 25 mL solution of methyl violet with a concentration of 30 mg/L (pH 7) was placed into 50 mL beaker glasses, and 20 mg each of  $\text{TiO}_2$ ,  $\text{TiO}_2/\text{analcime}$  zeolite, and  $\text{TiO}_2/\text{cancrinite}$  zeolite photocatalysts were added. The mixtures were then irradiated under UV light for 150 minutes. After irradiation, the absorbance of the solutions was measured using a UV-Vis spectrophotometer at the maximum wavelength of methyl violet.

## RESULTS AND DISCUSSION

### Preparation and activation of muscovite raw materials

The results of XRF muscovite raw material contain several metal oxides shown in Table 1, but there is a difference in concentration before

and after washing with 1M HCl, namely in  $\text{SiO}_2$  and  $\text{Al}_2\text{O}_3$ . The concentration of  $\text{SiO}_2$  after washing with 1M HCl increased while  $\text{Al}_2\text{O}_3$  decreased in concentration. According to Jia, et al. (2018), the calcination process was carried out at a temperature of 500 °C, causing the Al bond to break so that the concentration of  $\text{Al}_2\text{O}_3$  decreased, which then caused defects in the zeolite structure. The movement of less stable Si to occupy the position of Al that had been broken caused the concentration of  $\text{SiO}_2$  to increase from before being washed by 1M HCl.

According to Table 1, muscovite raw materials contain several metal oxides with noticeable differences in the concentrations of  $\text{SiO}_2$  and  $\text{Al}_2\text{O}_3$  before and after washing with 1M HCl. The concentration of  $\text{SiO}_2$  increased after washing, while  $\text{Al}_2\text{O}_3$  decreased. According to Jia et al. (2018), the calcination process at 500 °C disrupts Al bonds, leading to a reduction in  $\text{Al}_2\text{O}_3$  concentration and defects in the zeolite structure. The displacement of less stable Si atoms into the positions formerly occupied by Al results in an increase in  $\text{SiO}_2$  concentration after washing with 1M HCl. This observation is further supported by the diffraction pattern of muscovite raw materials before activation with 1M HCl, as shown in Figure 1.

Unactivated muscovite raw materials appear in muscovite, chlorite, and quartz peaks, some peaks  $2\theta = 5.88^\circ, 19.98^\circ, 28.92^\circ, 54.56^\circ,$  and  $62.14^\circ$  that appear on the sample can be changed by using 1M HCl, which functions as an activation agent to remove impurities present in the

**Table 1.** XRF results of muscovite raw materials before and after washing with 1M HCl

Metal oxide	Concentration (%) before washing with 1M HCl	Concentration (%) after washing with 1M HCl
$\text{SiO}_2$	49.293	50.888
$\text{Al}_2\text{O}_3$	46.114	44.831
$\text{Fe}_2\text{O}_3$	2.677	2.766
$\text{K}_2\text{O}$	0.920	0.782
$\text{TiO}_2$	0.511	0.513
CaO	0.310	0.064
MnO	0.049	0.046
$\text{ZrO}_2$	0.045	0.044
$\text{V}_2\text{O}_5$	0.021	0.020
$\text{Y}_2\text{O}_3$	0.015	0.010
$\text{Rb}_2\text{O}$	0.010	0.009
ZnO	0.008	0.008
CuO	0.008	0.007
SrO	0.008	0.004

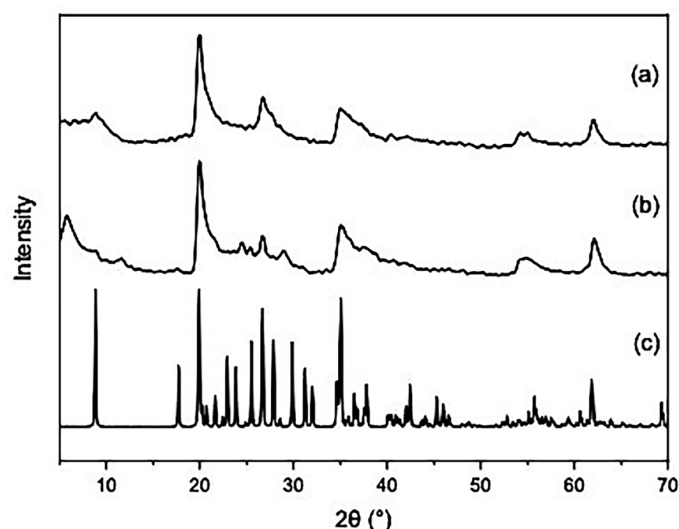


**Figure 1.** XRD diffraction patterns of a) activated muscovite raw materials, b) muscovite raw materials, and c) standard diffractogram for muscovite phase (COD file 96-901-2888).

sample (Tan, et al., 2017; Liu and Pan, 2013) to increase the surface area and open pores (Side, et al., 2023). Muscovite raw materials sample activated with 1M HCl (Figure 1a) is a crystalline mineral with the appearance of typical peaks at values  $2\theta = 19.99^\circ$ ,  $26.20^\circ$ ,  $34.99^\circ$ ,  $54.90^\circ$ , and  $62.02^\circ$ . Qualitative analysis can be identified by comparing the diffraction pattern of muscovite raw materials with the standard diffractogram of muscovite phase (COD file 96-901-2888). The typical peak of muscovite is at  $2\theta = 19.99^\circ$ , both samples have the typical peak.

This result is supported by the FTIR spectrum pattern of muscovite raw materials (Figure 2a), which shows the results of the FTIR spectrum of muscovite as reported in the research of Selim, et al. (2018), indicating peaks in the  $450\text{ cm}^{-1}$  to  $1100\text{ cm}^{-1}$  region of strong Si-O absorption and OH bending. According to previous reports, the  $468\text{ cm}^{-1}$  absorption is due to Si-O-Si bending vibrations and  $528\text{ cm}^{-1}$  Al-O-Al bending vibrations (Janek, et al., 2009). The  $694\text{ cm}^{-1}$  absorption band shows the Si-OH and  $912\text{ cm}^{-1}$  Al-OH functional groups. The absorption band around  $3400\text{ cm}^{-1}$  is a hydroxyl group (Herrera, et al., 2021). While in the FTIR spectrum pattern (Figure 2b), the peak in the  $450\text{--}1950\text{ cm}^{-1}$  absorption area has similarities to the mineral peak before activation, it indicates that washing using HCl does not damage the Si-O-Si and Al-O-Al structures (Liu and Pan, 2013) in muscovite raw materials used as a source of aluminosilicates in zeolite synthesis. According to Sabalova et al. (2018), 1M HCl can dissolve some of the mineral matrices and cause

structural changes in the sample, so that the wave numbers in  $2300\text{ cm}^{-1}$  to  $3400\text{ cm}^{-1}$  regions experience structural breakdown into several wave numbers caused by activation using 1M HCl (Alvand, et al., 2024).

### Synthesis zeolite from muscovite raw materials

This procedure generally involves the simultaneous addition and stirring of a solution containing muscovite raw materials, NaOH, and distilled water. Sodium hydroxide is used as the mineralizing agent (Wang, et al., 2007). Dissolution under hydrothermal conditions using  $\text{Na}_2\text{SiO}_3$ , CaOH, and KOH solutions has been studied (Ma et al., 2016). However, recrystallization of muscovite using NaOH solvent under hydrothermal conditions without organic templates is rarely reported.

Synthesis A, carried out at  $170^\circ\text{C}$  for 72 hours produced zeolite cancrinite as a single phase, by previous reports (Selim, et al., 2018; Ifeoma, et al., 2022), accompanied by significant diffraction peaks (Figure 3a), located at  $2\theta = 19.0^\circ$ ,  $24.0^\circ$ , and  $27.1^\circ$  which correspond to (110); (210); (211) peaks typical of zeolite cancrinite with standard cancrinite  $24.0^\circ$  (JCPDS No. 01-087-1523). Synthesis B produced analcime zeolite (Figure 3b) with sharp diffraction peaks  $2\theta = 15.8^\circ$ ,  $27.5^\circ$ , and  $30.9^\circ$  corresponding to crystal planes (211); (400); and (511) with standard analcime  $27.5^\circ$  (JCPDS No. 41-1478). This can be obtained by adjusting the Si/Al ratio. Therefore, the ratio affects the formation of crystal phase and crystallization of zeolite. Sodium

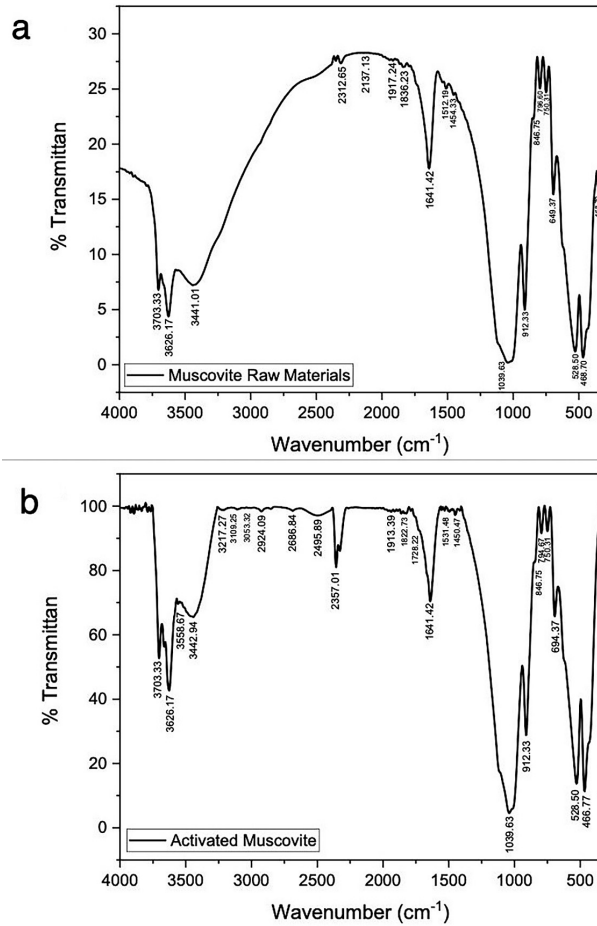


Figure 2. FTIR spectra of a) muscovite raw materials and b) 1M HCl activated muscovite

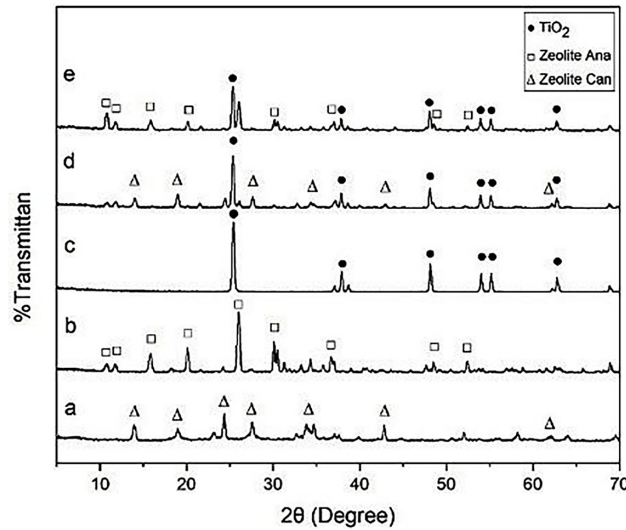


Figure 3. XRD Patterns (a) synthesis A, (b) synthesis B, (c) TiO<sub>2</sub> anatase, (d) TiO<sub>2</sub>-synthesis A, and (e) TiO<sub>2</sub>-synthesis B

hydroxide plays an important role in zeolite formation. Increasing the concentration of NaOH results in more SiO<sub>2</sub> forming cancrinite, so that the analcime phase changes to the cancrinite phase (Lee, et al., 2000).

### Fusing TiO<sub>2</sub> and synthetic zeolite

Figure 3c displays the TiO<sub>2</sub> anatase diffraction pattern, which was found on the crystal plane (101); (004); and (200) peaks. The usual peak

is  $2\theta = 25.3^\circ$ ,  $37.8^\circ$ , and  $48.1^\circ$  that appear like typical peaks of  $\text{TiO}_2$  anatase in the standard  $2\theta = 25.3^\circ$  (JCPDS No. 21-1272). The composites of  $\text{TiO}_2/\text{CAN}$  and  $\text{TiO}_2/\text{analcime}$  have been produced using a sonication method with a frequency of 20 KHz. The  $\text{TiO}_2/\text{cancrinite}$  composite in the diffraction pattern (3d) shows a significant indicator of composite formation at  $2\theta = 18.9^\circ$ ,  $25.3^\circ$ , and  $27.1^\circ$ . Adjacent peaks show typical  $\text{TiO}_2$  anatase and zeolite cancrinite patterns, suggesting that the intensity of the diffraction peak has not changed significantly, concluding that zeolite cancrinite molecules have no influence (Ifeanyi, et al., 2024). In diffraction pattern (3e),  $\text{TiO}_2/\text{analcime}$  photocatalyst shows a sharp peak at  $2\theta = 20.1^\circ$ ,  $25.3^\circ$ ,  $30.1^\circ$  and undergoes some shifts due to the presence of a new  $\text{TiO}_2$  anatase phase, which has a distinctive peak of  $25.3^\circ$ . However, the characteristic peaks of analcime and cancrinite also appear, although they are slightly shifted due to the composite process. However, it still indicates that the zeolite structure was not significantly damaged during the synthesis process. However, the zeolite (analcime) peaks are weak, which can be explained by the low zeolite concentration of the composite and the fact that  $\text{TiO}_2$  nanoparticles assemble the zeolite surface, which lowers the ANA zeolite peak in the composite. (Saule, et al., 2024).

The infrared spectra of synthesized  $\text{TiO}_2/\text{analcime}$  and  $\text{TiO}_2/\text{cancrinite}$  are shown in Figure 4, and the spectra bands correspond to aluminosilicate and anatase  $\text{TiO}_2$  materials. The absorption band  $450\text{--}600\text{ cm}^{-1}$  is the O-Ti-O stretching vibration

by standard (NIST 13463-67-7). While  $610\text{--}1100\text{ cm}^{-1}$  corresponds to bending vibrations (TO<sub>4</sub>, T=Si/Al), Si-O-Ti asymmetric vibrations and Ti-O deformation confirm titanium presence in the material structure. This band stretches to a band with  $\text{H}_2\text{O}$  bending vibrations at about  $3000\text{ cm}^{-1}$  from the region around  $1300\text{ cm}^{-1}$ . The stretching vibration of the hydroxyl group is represented by the absorption band at  $3000\text{--}3600\text{ cm}^{-1}$  (Amin, et al., 2023). Overall, these FTIR results confirm the successful impregnation of  $\text{TiO}_2$  on the zeolite without damaging the main structure of the material.

The morphology of  $\text{TiO}_2$  with zeolite ANA and CAN at various magnifications is displayed in Figure 5. Figure 5c displays a uniform size of  $10.58\text{ }\mu\text{m}$  and a characteristic hexagonal structure of  $\text{TiO}_2/\text{ANA}$  (Figure 5a,b). Most crystals with the same shape were also found in kaolinitic rock zeolite analcime (Novembre and Gimeno, 2021), and fly ash zeolite analcime (Li, et al., 2023).  $\text{TiO}_2/\text{CAN}$  (Figure 5d,e) exhibits a cancrinite-typical shape as rod-like, hexagonal needles in Figure 5f, which have a length of roughly  $21.3\text{ }\mu\text{m}$ . Similar morphologies were found in cancrinite zeolites synthesized from a geophagic clay (Joseph, et al., 2022), and cancrinite in sediment (Deng, et al., 2006). The morphological results for  $\text{TiO}_2$  are in the form of amorphous nanoparticles only thinly distributed over the zeolite, because the material ratio in the synthesis (10 g zeolite vs. 4 g  $\text{TiO}_2$ ) is dominated by zeolite, which can cause  $\text{TiO}_2$  not to be visible morphologically, the  $\text{TiO}_2$  particles have a round shape and size and uniform morphology

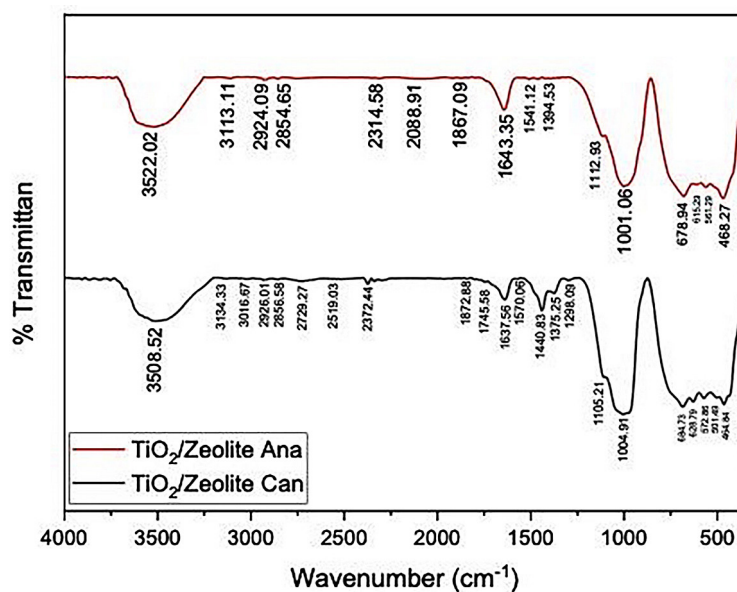
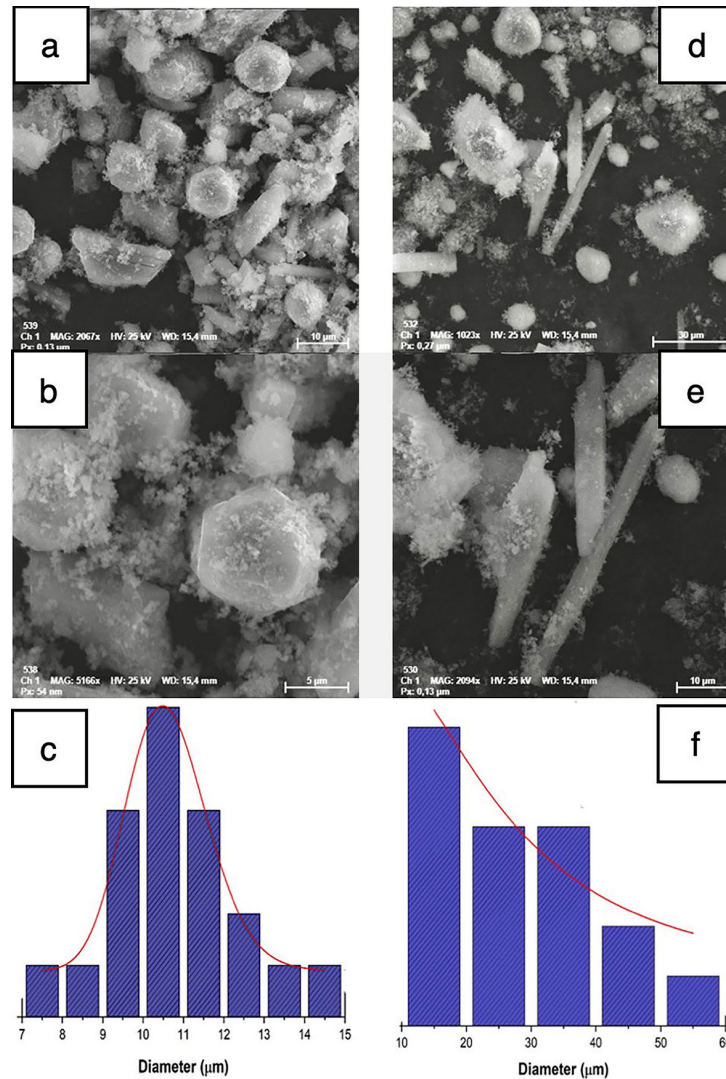


Figure 4. FTIR Spectra of  $\text{TiO}_2/\text{cancrinite}$  and  $\text{TiO}_2/\text{analcime}$  composites



**Figure 5.** TiO<sub>2</sub>/ANA composite (a-c) and TiO<sub>2</sub>/CAN composites, (d-f) SEM photos at varying magnifications

(Tovani, et al., 2020). SEM analysis showed that some of the small particles surrounding the zeolite were TiO<sub>2</sub> in the anatase phase based on their size and distribution. This is supported by anatase TiO<sub>2</sub> which is often formed as small particles. According to Shokry et al. (2025), the SEM analysis of TiO<sub>2</sub> found that TiO<sub>2</sub> particles are mostly spherical with diameters ranging from 70 to 158 nm.

The surface area and pore size distribution of the TiO<sub>2</sub>/CAN and TiO<sub>2</sub>/ANA composites, as determined by N<sub>2</sub> adsorption, exhibit a similar pattern in Figure 6, with a sharp increase in spike at relatively low pressure (P/Po) followed by a narrow hysteresis at P/Po = 0.8 – 1.0 due to the solid surface pores controlling capillary condensation and the number of adsorbate layers (Toshihide and Nicholson, 2011), and is associated with solids having particle aggregates containing slit-shaped pores. Composite exhibits a type-III

isotherm (Burhan, et al., 2018). Table 2 shows the pore size > 2 nm using the BJH method, and the composite obtained a mesoporous structure (Dey, et al., 2023). Cancrinite and analcime zeolites with TiO<sub>2</sub> addition significantly increased surface area. Previous studies revealed the surface areas of cancrinite and analcime to be 14.71 m<sup>2</sup>/g and 17.39 m<sup>2</sup>/g, respectively (Amin, et al., 2023). These findings offer a fascinating perspective on the impact of TiO<sub>2</sub> addition, which is known as a semiconductor material with high photocatalytic activity that not only provides additional functionality but also affects the pore of zeolite, further increasing the presence of TiO<sub>2</sub> addition. The BJH adsorption surface area of the TiO<sub>2</sub>/ANA composite is 48.64 m<sup>2</sup>/g, while that of the TiO<sub>2</sub>/CAN sample is 32.20 m<sup>2</sup>/g. The mesopore surface area gives a higher estimate, because BJH method calculates the total area of the mesopores.

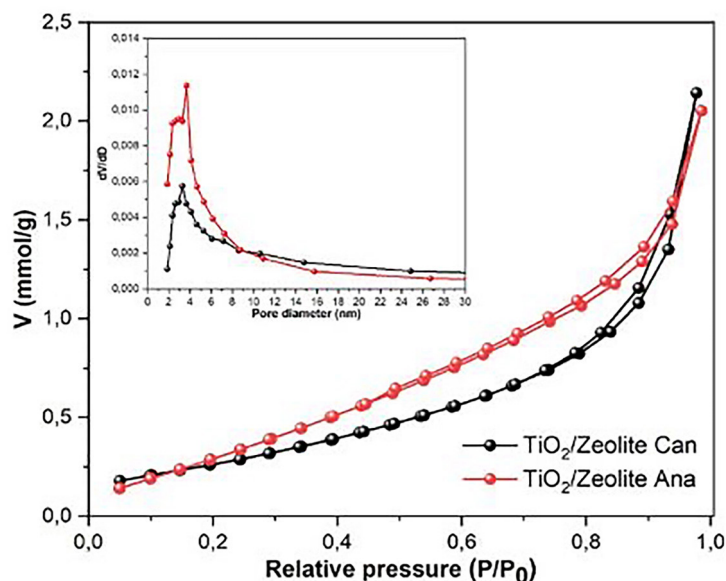


Figure 6. The composites by isothermal  $N_2$  adsorption-desorption and pore size distribution (as an inset figure)

Table 2. The result of composites using the BET method

Composites	Surface area	Pore diameter	Total pore volume
TiO <sub>2</sub> /ANA	34.80 m <sup>2</sup> /g	8.2 nm	0.07 cm <sup>3</sup> /g
TiO <sub>2</sub> /CAN	23.08 m <sup>2</sup> /g	12.9 nm	0.07 cm <sup>3</sup> /g

Figure 7 shows the UV-Vis reflectance spectrum with the determination of band gap energy, which can be obtained by plotting a straight line that intersects the X-axis on the graph of the relationship between energy (eV) with  $(F(R)hv)^{1/2}$ . This graph shows anatase TiO<sub>2</sub> has a band gap

energy = 3.17 eV approach to the band gap energy of previous research (Zhuang, et al., 2022). The decrease in the TiO<sub>2</sub>/CAN (3.13 eV) and TiO<sub>2</sub>/ANA (3.11 eV) composites indicates structure modification due to the interaction between TiO<sub>2</sub> and zeolite. The TiO<sub>2</sub>/ANA composite, with the

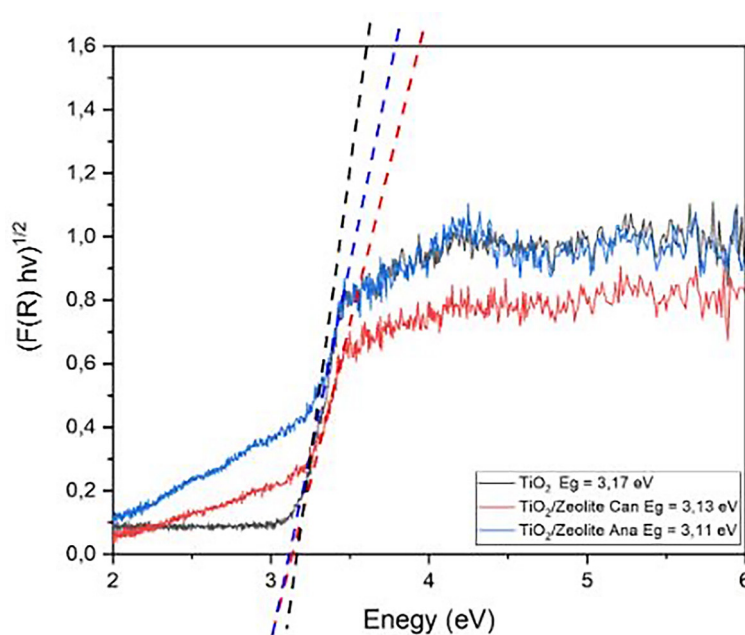


Figure 7. Band gap determination graphs of TiO<sub>2</sub> anatase, TiO<sub>2</sub>/CAN and TiO<sub>2</sub>/ANA composites



lowest band gap value, shows the most significant interaction between  $\text{TiO}_2$  and zeolite analcime. This is likely due to the nature of analcime zeolite, which supports the even dispersion of  $\text{TiO}_2$ , thereby increasing charge transfer and lowering the electron excitation energy. This decrease in band gap energy indicates that both composites have a higher potential to utilize UV light with a larger wavelength (Irodia, et al., 2023) than  $\text{TiO}_2$  anatase without supporting materials so that the  $\text{TiO}_2/\text{ANA}$  photocatalyst is more effective for photodegradation activity tests and can be proven by the photocatalytic test results in Figure 8. When  $\text{TiO}_2$  is distributed in zeolite, there is interaction between  $\text{TiO}_2$  and zeolite at their interface. These interactions can change the interface structure and affect the electron energy levels in  $\text{TiO}_2$ . A modification in the band gap energy distribution in  $\text{TiO}_2$  results in a reduction of the band gap.

### Photocatalytic test

In the photodegradation effectiveness test stage, testing was carried out under optimum conditions using  $\text{TiO}_2/\text{ANA}$ ,  $\text{TiO}_2/\text{CAN}$ , and  $\text{TiO}_2$ . This comparison aims to evaluate the effectiveness of adding  $\text{TiO}_2/\text{ANA}$  in degrading methyl violet compared to using  $\text{TiO}_2$  and  $\text{TiO}_2/\text{CAN}$ . The results of testing the effectiveness of methyl violet photodegradation for each treatment can be seen in Figure 8.

According to statistics, the percentage of degradation using  $\text{TiO}_2$  is obtained at 50.48%, this is

due to the ability of  $\text{TiO}_2$  as a semiconductor to decompose methyl violet through the mechanism of absorption of UV radiation.  $\text{TiO}_2$  can decompose methyl violet in the UV absorption region with a band gap of 3.17 eV. The semiconductor nature of  $\text{TiO}_2$  allows this material to absorb light energy, especially UV radiation, thus producing electron and hole pairs that trigger the formation of hydroxyl radicals ( $\bullet\text{OH}$ ) (Shokry, et al., 2025). In the photodegradation treatment using  $\text{TiO}_2/\text{CAN}$ , the degradation percentage increased to 91.66%. This increase is due to the modification of  $\text{TiO}_2$  on the surface of zeolite cancrinite, which reduces the band gap of  $\text{TiO}_2$  from 3.17 eV to 3.13 eV. This decrease in band gap reduces the energy required for electron transition from the valence band to the conduction band, thereby increasing the degradation efficiency (Katwal, et al., 2021). Meanwhile, using  $\text{TiO}_2/\text{ANA}$  produced the highest degradation percentage of 95.33%. This efficiency is influenced by the modification of  $\text{TiO}_2$  on zeolite analcime, which functions as a carrier to expand the specific surface and improve the distribution of  $\text{TiO}_2$  (Huayna, et al., 2024). On the basis of supporting data,  $\text{TiO}_2/\text{ANA}$  has a band gap of 3.11 eV and a larger surface area than  $\text{TiO}_2/\text{CAN}$ , contributing to higher degradation effectiveness. Thus, the development of  $\text{TiO}_2$  on the surface of zeolites, especially analcime zeolites, was shown to improve the photodegradation efficiency by decreasing the band gap and optimizing the surface area.

Table 3 compares the photocatalytic degradation performance in degrading methyl violet of

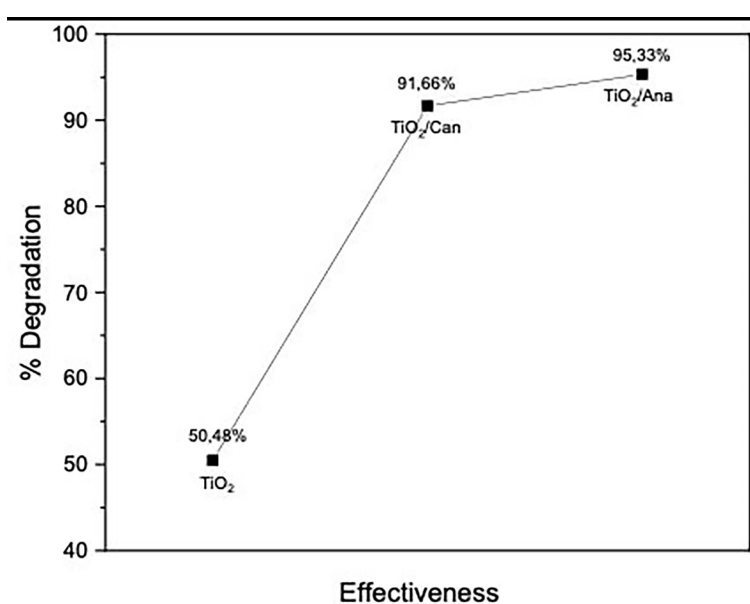


Figure 8. Graph of methyl violet photodegradation effectiveness test

various catalyst systems under different experimental conditions, highlighting the differences in catalyst type, methyl violet concentration, catalyst mass, irradiation time, and maximum percent

degradation of methyl violet. This table shows the efficiency of this study, which reached 97.23% on TiO<sub>2</sub>/ANA, 95.33% degradation using TiO<sub>2</sub>/ANA, and 91.66% degradation on TiO<sub>2</sub>/CAN in

**Table 3.** Comparison of photocatalytic degradation performance in degrading methyl violet of various catalyst systems under different experimental conditions

Catalyst	Catalyst dosage (g)	Concentration of MV (mg/L)	Time (minute)	Percentage (%) degradation	Ref
TiO <sub>2</sub> /ANA/UV	0.02	30	150	95.33	Present work
TiO <sub>2</sub> /CAN/UV	0.02	30	150	91.66	Present work
TiO <sub>2</sub> /UV	1	10	14	89	Shokry, et al., 2025
TiO <sub>2</sub> /natural light	0.3	20	30	83	Yang, et al., 2013
TiO <sub>2</sub> /Pt/UV	0.025	15	20	72.6	Saeed, et al., 2017
Pristine TiO <sub>2</sub> /UV	-	-	480	70	Padma, et al., 2023
CuO-TiO <sub>2</sub>	1	-	480	49.5	Sherly, et al., 2024
TiO <sub>2</sub> /AgNP/UV	-	4	100	89	Oliveira and Sant'Ana., 2024
Au/UV	-	-	180	86	Gadallah, et al., 2007

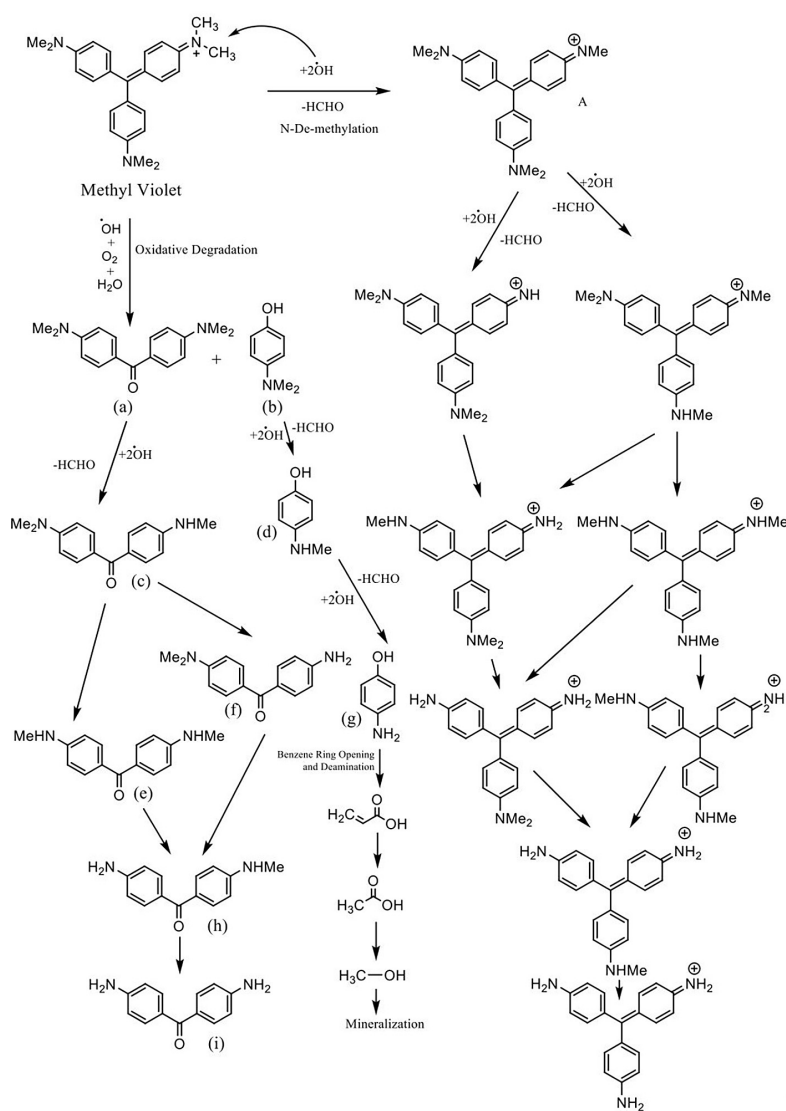


**Figure 9.** Reaction mechanism of methyl violet degradation process

the degradation of methyl violet using 20 mg in each catalyst variation under UV light for 150 minutes. This performance surpasses many other studies, including those using advanced catalysts such as Pt metal-doped TiO<sub>2</sub>, which often require longer times or higher costs. Alternative systems, such as TiO<sub>2</sub> using a recirculating reactor (Shokry, et al., 2025), show good efficiency but involve aluminum foil as a UV light enhancer in the reactor. Compared to this study, the combination of TiO<sub>2</sub>/zeolite is efficient in degrading methyl violet due to the utilization of natural resources, and its high efficiency emphasizes its potential as a cost-effective and environmentally friendly solution for color effluent treatment.

The mechanism of methyl violet degradation using photocatalysts involves a series of oxidation and de-methylation reactions initiated by forming hydroxyl radicals (•OH) on the photocatalyst surface (Haleem, et al., 2024). The reaction starts with N-demethylation, releasing the methyl group on the methyl violet molecule, producing formaldehyde (HCHO) as a by-product. In the final stage, this reaction gradually produces simple organic compounds, such as HCOOH and CH<sub>3</sub>OH, which are mineralized to carbon dioxide (CO<sub>2</sub>) and water (H<sub>2</sub>O). This process demonstrates the efficiency of photocatalysts in degrading complex molecules into simpler and environmentally friendly products (Fig. 9).

## CONCLUSIONS

In this study, the hydrothermal method was successfully used to make synthetic zeolites from raw materials of muscovite into cancrinite and analcime zeolites. In principle, the formation of various types of zeolites can be designed by selecting the temperature and alkali concentration used. Then, they are composited with anatase TiO<sub>2</sub> to become a more effective photocatalyst in degrading methyl violet dye. The TiO<sub>2</sub>/ANA photocatalysts showed hexagonal morphology with homogeneous crystals with a surface area of 34.80 m<sup>2</sup>/g. In contrast, TiO<sub>2</sub>/CAN showed a rod morphology with a surface area of 23.08 m<sup>2</sup>/g, each morphology surrounded by small particles indicating the morphology of TiO<sub>2</sub>. UV-DRS spectra confirmed that TiO<sub>2</sub>/ANA showed a lower band gap of 3.11 eV compared to TiO<sub>2</sub> (3.17 eV) and TiO<sub>2</sub>/CAN (3.13 eV). The TiO<sub>2</sub>/zeolite ANA composite showed photocatalytic efficiency in

degrading methyl violet with a dye degradation of 95.33%. This experiment proves that TiO<sub>2</sub>/zeolite-based photocatalyst can be used to treat dye-contaminated wastewater, contributing to environmental sustainability.

## Acknowledgment

This research is fully supported by BIMA Kemendikbudristek. The author would like to thank the Directorate of Research, Technology, and Community Service of the Directorate General of Higher Education, Research, and Technology with Hasanuddin University in 2024, contract number: 050/E5/PG.02.00.PL/2024, dated June 11, 2024.

## REFERENCES

1. Aichour, A., Djafer, K.H., and Zaghouane, B.H. (2021). Textile dyes removal from wastewater using recent promising composites: A review. *Algerian Journal of Chemical Engineering* 2: 49–65. <https://doi.org/10.5281/zenodo.5451775>
2. Alvand, M., Ma, Z., Kokate, R., Kumar, P.V., Pan, J., Amal, R., Lovell, E.C., and Jalili, A.R. (2024). Uncovering the role of vanadium-doped Ni<sub>2</sub>P for low concentration urea oxidation. *Chemical Engineering Journal*. 500: 157130. <https://doi.org/10.1016/j.cej.2024.157130>
3. Amin, I.I., Wahab, A. W., Mukti, R.R., and Taba, P. (2023). Synthesis and characterization of zeolite type ANA and CAN framework by hydrothermal method of Mesawa natural plagioclase feldspar. *Applied Nanoscience*. pages 1-10. <https://doi.org/10.1007/s13204-022-02756-4>
4. Berradi, M., Hsisou, Rachid, Khudhair, M., Assouag, M., Cherkaoui, O., Bachiri, A. E., and Harfi, A, E. (2019). Textile finishing dyes and their impact on aquatic environs: a review. *Heliyon*. 5: e02711. Pages1-11. <https://doi.org/10.1016/j.heliyon.2019.e02711>
5. Bouasla, C., Samar, M. E. H., and Ismail, F. (2010). Degradation of methyl violet 6B dye by the fenton process. *Desalination* 254. 35–41. <https://doi.org/10.1016/j.desal.2009.12.017>
6. Burhan, M., Wakil, M., and Ng, K.C. 2018. Energy distribution function based universal adsorption isotherm model for all types of isotherms. *International Journal of Low-Carbon Technologies* 13: 292–297. <https://doi.org/10.1093/ijlct/cty031>
7. Deng, Y., Flury, M., Harsh, J.B., Felmy, A.R., and Qafoku, O. (2006). Cancrinite and sodalite formation in the presence of cesium, potassium, magnesium, calcium and strontium in Hanford tank waste

- simulants. *Applied Geochemistry*. 2049–2063. <https://doi.org/10.1016/j.apgeochem.2006.06.019>
8. Derbe, T., Temesgen, S., and Bitew M. (2021). A Short Review on Synthesis, Characterization, and Applications of Zeolites. *Advances in Materials Science and Engineering*. 6637898: 1–17. <https://doi.org/10.1155/2021/6637898>
9. Dey, A., Varagnolo, S., Power, N.P., Vangapally, N., Elias, Y., Dampthey, L., Jaato, B.N., Gopalan, S., Golrokhi, Z., Sonar, P., Selvaraj, V., Aurbach, D., and Krishnamurthy, S. (2023). Doped MXenes—A new paradigm in 2D systems: Synthesis, properties and applications. *Progress in Materials Science*. 139: 101166 1–70. <https://doi.org/10.1016/j.pmatsci.2023.101166>
10. Dharma, H.N.C., Jaafar, J., and Widiastuti, N. (2022). A Review of titanium dioxide (TiO<sub>2</sub>)-based photocatalyst for oilfield-produced water treatment. *Membranes*. 12: 345. <https://doi.org/10.3390/membranes12030345>
11. Doğaroğlu, Z.G., Uysal, Y., Demir, A., Makas, M.N., & Çaylalı, Z. (2023). Synthesis, characterization, and optimization of PVA/SA hydrogel functionalized with zeolite (clinoptilolite): Efficient and rapid color removal from complex textile effluents. *Materials Chemistry and Physics*, 295, 127090. <https://doi.org/10.1016/j.matchemphys.2022.127090>
12. Gadallah, T.A., S. Kato, S. Satokawa, T. Kojima. (2007). Role of core diameter and silica content in photocatalytic activity of TiO<sub>2</sub>/SiO<sub>2</sub>/Fe<sub>3</sub>O<sub>4</sub> composite, *Solid State Sci*. 9(8): 737–743. <https://doi.org/10.1016/j.solidstatesciences.2007.05.012>
13. Haleem, A., Ullah, M., Rehman, S., Shah, A., Farooq, M., Saeed, T., Ullah, I., and Li, H. (2024). In-depth photocatalytic degradation mechanism of the extensively used dyes malachite green, methylene blue, congo red, and Rhodamine B via covalent organic framework-based photocatalysts. *Water* 16, 1588. <https://doi.org/10.3390/w16111588>
14. Herrera, C.A.R., Cruz-Cruz, I., Cedenó, I.H.J., Romero, O.M., and Zuniga, A.E. (2021). Influence of the epoxy resin process parameters on the mechanical properties of produced bidirectional [±45°] carbon/epoxy woven composites. *Polymers* 13: 1273. <https://doi.org/10.3390/polym13081273>
15. Huang, C., Ding, Y., Chen, Y., Li, P., Zhu, S., and Shen, S. (2017). Highly efficient Zr doped-TiO<sub>2</sub>/glass fiber photocatalyst and its performance in formaldehyde removal under visible light. *Journal of Environmental Sciences*. 60, 61–69. <https://doi.org/10.1016/j.jes.2017.06.041>
16. Huayna, G., Laura, A., Churata, R., Lazo, L., Guzman, R., Ramos, P.G. and Rodeiguez J.M. (2024). Synthesis and characterization of a photocatalytic material from TiO<sub>2</sub> nanoparticles supported on zeolite obtained from ignimbrite residue used in decolorization of methyl orange. *Appl. Sci*. 14: 3146. <https://doi.org/10.3390/app14083146>
17. Ifeanyi, M.S.A., Bilainu, O., and Yusuf, M.I. (2024). Effects of transition metal doping on the properties and catalytic performance of ZSM-5 zeolite catalyst on ethanol-to-hydrocarbons conversion. *Fuel Communications*. 18: 100101. 1–11. <https://doi.org/10.1016/j.fueco.2023.100101>
18. Ihaddaden, S., Aberkane, D., Boukerroui, A., and Robert, D. (2022). Removal of methylene blue (basic dye) by coagulation-flocculation with biomaterials (bentonite and Opuntia ficus indica). *Journal of Water Process Engineering*. 49: 102952. <https://doi.org/10.1016/j.jwpe.2022.102852>
19. Irodia, R., Ungureanu, C., Satulu, V., and Mindroiu, V.M. (2023). Photocatalyst Based on nanostructured TiO<sub>2</sub> with improved photocatalytic and antibacterial properties. *Materials*. 16: 7509. 1–22. <https://doi.org/10.3390/ma16247509>
20. Isik, M. Z., Saleh, I., M'barek, E. Yabalak, N. Dizge and B. Deepanraj. (2022). Investigation of the adsorption performance of cationic and anionic dyes using hydrochared waste human hair. *Biomass Conversion Biorefinery*. 1–14. <https://doi.org/10.1007/s13399-022-02582-2>
21. Janek, M., Bugar, I., Lorenc, D., Szocs, V., Velic, D., Chorvat, D. (2009). Terahertz Time-Domain Spectroscopy of Selected Layered Silicates. *Clays and Clay Minerals*, 57(4): 416–424. <https://doi.org/10.1346/CCMN.2009.0570402>
22. Jeyasubramaniana, K., Hikku., G.S. and Krishna Sharma R. (2015). Photocatalytic degradation of methyl violet dye using zinc oxide nanoparticles prepared by a novel precipitation method and its anti-bacterial activities. *Journal of Water Process Engineering* 8, 35–44. <https://doi.org/10.1016/j.jwpe.2015.08.007>
23. Joseph, I. V., Doyle, A.M., Amedlous, A., Mintova, S., and Tosheva, L. (2022). Scalable solvent-free synthesis of aggregated nanosized single-phase cancrinite zeolite. *Materials Today Communications*. 32: 103879. 1–7. <https://doi.org/10.1016/j.mtcomm.2022.103879>
24. Karaman, O. Karaman, P.-L. Show, H. Karimi-Maleh and N. Zare. (2022). Congo red dye removal from aqueous environment by cationic surfactant modified-biomass derived carbon: Equilibrium, kinetic, and thermodynamic modeling, and forecasting via artificial neural network approach. *Chemosphere*. 290: 133346. <https://doi.org/10.1016/j.chemosphere.2021.133346>
25. Katwal, R. Kothari and D. Pathania. (2021). Chapter 10 - An overview on degradation kinetics of organic dyes by photocatalysis using nanostructured electrocatalyst. *Delivering Low-Carbon Biofuels with Bioproduct Recovery*. 195–213. <https://doi.org/10.1016/j.chemosphere.2021.133346>

- [org/10.1016/B978-0-12-821841-9.00005-0](https://doi.org/10.1016/B978-0-12-821841-9.00005-0)
26. Khaleque, A., Alam, M. M., Hoque, M., Mondal, S., Haeder, J.B., Xu, B., Johir, M.A.H., Karmakar, A.K., Zhou, J.L., Ahmed, M.B., Moni, M.A. (2020). Zeolite synthesis from low-cost materials and environmental applications. A review. *Environmental Advances*. 2: 100019. <https://doi.org/10.1016/j.envadv.2020.100019>
  27. Kim, S.J., Kim, E.M., H.K. Jeon., S.B. Kale., J.Y. Choi., and J.H. Kim. (2022). Photoreactor-Initiated Acetaldehyde Conversion Rate of a TiO<sub>2</sub>-Surface-Treated Alumina Photocatalyst Prepared Using the Sol-Gel Method. *Appl. Sci.* 12: 5796. <https://doi.org/10.3390/app12125796>
  28. Lee, M.G., Yi, G., Ahn, B.J., and Roddick, F. (2000). Conversion of Coal Fly Ash into Zeolite and Heavy Metal Removal Characteristics of the Products. *Korean J. Chem. Eng.*, 17(3), 325–331. <https://doi.org/10.1007/BF02699048>
  29. Li, S., Jia, S., Nagasaka, T., Bai, H. and Yang, L. (2023). CO<sub>2</sub> adsorption properties of amine-modified zeolites synthesized using different types of solid waste. *Sustainability*. 5: 10144. 1–17. <https://doi.org/10.3390/su151310144>
  30. Liu Y., and Pan, H. (2013). Hydrogen Storage Materials. *New and Future Developments in Catalysis, Batteries, Hydrogen Storage and Fuel Cells*. 377–405. <https://doi.org/10.1016/B978-0-444-53880-2.00018-1>
  31. Ma, X., Yang, J., Ma, H., and Liu, C. (2016) Hydrothermal extraction of potassium from potassic quartz syenite and preparation of aluminum hydroxide. *Int J Miner Process* 147: 10–17. <https://doi.org/10.1016/j.minpro.2015.12.007>
  32. Maj, I., and Matus, K. (2023). aluminosilicate clay minerals: kaolin, bentonite, and halloysite as fuel additives for thermal conversion of biomass and waste. A Review. *Energies*. 16: 4359. <https://doi.org/10.3390/en16114359>
  33. Nikravesh, B., Shomalnasab, A., Nayyer, A., Aghababaei, N., Zarebi, R., and Ghanbaru, F. (2020). UV/Chlorine Process for dye degradation in aqueous solution: Mechanism, affecting factors, and toxicity evaluation for textile wastewater. *Journal of Environmental Chemical Engineering*. 8(5): 104244. <https://doi.org/10.1016/j.jece.2020.104244>
  34. Novembre, D. and Gimeno, D. (2021). Synthesis and characterization of analcime (ANA) zeolite using a kaolinitic rock. *Scientific Reports*. 11:13373, 1–10. <https://doi.org/10.1038/s41598-021-92862-0>
  35. Oliveira, R.de., and Sant’Ana, A.C. (2024). Crystal Violet degradation by visible light-driven AgNP/TiO<sub>2</sub> hybrid photocatalyst tracked by SERRS spectroscopy. *Vibrational Spectroscopy*, 133: 103694. <https://doi.org/10.1016/j.vibspec.2024.103694>
  36. Padma, C.M., Raja, D.H., and Davidson, D.J. (2023). Photodegradation of Methyl violet using Ag modified TiO<sub>2</sub> nanotubes by UV and UV/H<sub>2</sub>O<sub>2</sub>. *Chem. Phys. Impact* 7: 100366. <https://doi.org/10.1016/j.chphi.2023.100366>
  37. Pal, A., Jana, T.K., and Chatterjee, K. (2016). Silica supported TiO<sub>2</sub> nanostructures for highly efficient photocatalytic application under visible light irradiation. *Materials Research Bulletin*. 76, 353–357. <https://doi.org/10.1016/j.mattersbull.2015.12.040>
  38. Perwez, M., Fatima, H., Arshad, M., V. Meena, and B. Ahmad. (2022). Magnetic iron oxide nanosorbents effective in dye removal. *Int. Journal of Environmental Science and Technology*. 20(5), 1–18. <https://doi.org/10.1007/s13762-022-04003-3>
  39. Porcu, S., Secci, F., and Ricci, P.C. (2022). Advances in hybrid composites for photocatalytic applications: A review. *Molecules*. 27: 6828. <https://doi.org/10.3390/molecules27206828>
  40. Sadiku, M., Selimi, T., Berisha, A., Maloku, A., Mehmeti, V., Thaci, V., and Hasani, N. (2022). Removal of methyl violet from aqueous solution by adsorption onto halloysite nanoclay: Experiment and theory. *Toxics*. 10: 445. 1–19. <https://doi.org/10.3390/toxics10080445>
  41. Saeed, K., Khan, I., Gull, T., and M. Sadiq. (2017). Efficient photodegradation of methyl violet dye using TiO<sub>2</sub>/Pt and TiO<sub>2</sub>/Pd photocatalysts. *Appl. Water Sci.* 7 3841–3848. <https://doi.org/10.1007/s13201-017-0535-3>
  42. Saule, M., Zhanibek, A., Milana, B., John, V., Dionissios, M., Timur, S.A., and Stavros, G.P. (2024). TiO<sub>2</sub>/Zeolite Composites for SMX Degradation under UV Irradiation. *Catalysts*. 14: 147. 1–16. <https://doi.org/10.3390/catal14020147>
  43. Selim, A.Q., Mohamed, E.A., Seliem, M.K., Zayed, A.M. (2018). Synthesis of sole cancrinite phase from raw muscovite: Characterization and optimization. *Journal of Alloys and Compounds*, 762: 653–667. <https://doi.org/10.1016/j.jallcom.2018.05.195>
  44. Sherly, R.A., Padma, C.M., D.H. Raja, S. Sindhu-sha, A.I. Almansour, S.S.J. Dhas. (2024). H<sub>2</sub>O<sub>2</sub>-assisted photo-electrocatalytic and photocatalytic degradation of methyl violet by CuO-modified TiO<sub>2</sub> nanotube arrays. *Opt. Mater. (Amst)* 155: 115870.
  45. Shokry, F., El-Gedawy, M., Nosier, S. A., Aziz, M. A. H. (2025). Optimizing photocatalytic degradation of methyl violet dye in a recirculating slurry-type reactor. *Results in Chemistry* 13: 101980. <https://doi.org/10.1016/j.rechem.2024.101980>
  46. Side, S., Putro, S.E., Pratiwi, D.E., Rahma, A., and Rahman, A. 2023. The effect of acid treatment on the characteristics of modernite zeolite. *Jurnal Sainsmat*, 12(2): 114-123.
  47. Singh, A., Pal, D. B., M. Akbar., Alhazmi, A., Haque, S., Yoon, T., Srivastava, N., and Gepta, V. K. (2022). Biological remediation technologies for dyes and

- heavy metals in wastewater treatment: New insight. *Bioresource Technology*. 343: 126154. <https://doi.org/10.1016/j.biortech.2021.126154>
48. Velarde, L., Akhtar, F., & Inglezakis, V.J. (2023). Adsorption of heavy metals on natural zeolites: A review. *Chemosphere*, 328, 138508. <https://doi.org/10.1016/j.chemosphere.2023.138508>
49. Wang, Y., Lin, M., and Tuel, A. (2007). Hollow TS-1 crystals formed via a dissolution–recrystallization process. *Microporous and Mesoporous Materials*. 102: 80–85. <https://doi.org/10.1016/j.micromeso.2006.12.019>
50. Zhang, P., O'Connor, D., Wang, Y., Jiang, L., Xia, T., Wang, L., Tsang, D.C., Ok, Y.S., Hou, D. A green biochar/iron oxide composite for methylene blue removal. (2020). *J. Hazard. Mater.* 384: 121286. <https://doi.org/10.1016/j.jhazmat.2019.121286>
51. Zhang, S., Zhang, J., Sun, J., and Tang, Z. (2020). Capillary microphotoreactor packed with TiO<sub>2</sub>-coated glass beads: An efficient tool for photocatalytic reaction. *Chemical Engineering and Processing – Process Intensification*. 147: 107746. <https://doi.org/10.1016/j.cep.2019.107746>
52. Zhou, H., Wang, H., Yue, C., He, L., Li, H., Zhang, H., Yang, S. and Ma, T. (2024). Photocatalytic degradation by TiO<sub>2</sub>-conjugated/coordination polymer heterojunction: Preparation, mechanisms, and prospects. Review. *Applied Catalysis B: Environment and Energy*. 344: 123605. <https://doi.org/10.1016/j.apcatb.2023.123605>
53. Zhuang, Q. Zhu, G. Li, Z. Wang, P. Zhan, C. Ren, Z. Si, S. Li, D. Cai dan P. Qin. (2022). Photocatalytic degradation of organic dyes using covalent triazine-based framework. *Mater. Res. Bull.* 146: 111619. <https://doi.org/10.1016/j.materresbull.2021.111619>